PIER C

(Received 6 August 2026, Accepted 1 September 2026, Scheduled 13 September 2026)

Graphene-Based Multi-Band Reconfigurable Terahertz Antenna with Wide Tuning Range

Khalid S. Ahmad[1,*], Muhammad Inam Abbasi[2,*], Ahmed J. A. Al-Gburi[3], and Mohamad Z. A. Abd Aziz[2]

[1]*Department of Electronic Engineering and Communications Technologies*
Polytechnic College Mosul, Northern Technical University (NTU), Mosul 41001, Iraq
[2]*Faculty of Electronics and Computer Engineering and Technology*
Universiti Teknikal Malaysia Melaka, Melaka 76100, Malaysia
[3]*Strategic Research Institute (SRI), Asia Pacific University*
Jalan Teknologi 5, Taman Teknologi Malaysia, Kuala Lumpur 57000, Malaysia

ABSTRACT: This work demonstrates the design of a terahertz (THz) antenna that uses graphene to achieve frequency-reconfigurable multiband operation. The proposed design integrates electrically controlled graphene switches within precisely defined slots to dynamically modify the distribution of surface currents, enabling a highly multi-band, frequency-reconfigurable antenna. The antenna consists of perpendicular (vertical and horizontal) slots, supported by six graphene switches, whose operating frequencies are adjusted by controlling the graphene's chemical potential. The proposed antenna covers a wide frequency range from 0.288 to 2.501 THz, operating at 63 resonant frequencies and 58 impedance bands, achieved through 11 reconfiguration states (C1–C11). The proposed antenna is created on a 10 μm-thick Rogers RO3003 substrate with overall dimensions of 268 μm × 240 μm × 10 μm. The performance of the proposed antenna, including the reflection coefficient, gain, and radiation efficiency, was evaluated under different operating conditions. Due to its ability to reconfigure multiple frequency bands, this antenna is an ideal solution for dynamically adjustable, tunable THz communication systems.

1. INTRODUCTION

Reconfigurable antennas keep pace with the rapid growth of wireless communication systems, making them a major focus of contemporary scientific research. Reconfigurable antennas are characterized by their ability to dynamically modify frequency, radiation patterns, or polarization with no noticeable delay in response. In contrast, conventional antennas are limited to fixed and predetermined frequency bands, radiation characteristics, and polarizations [1–3]. Frequency-reconfigurable antennas occupy a prominent place in contemporary research, as they offer high adaptability in frequency management and enhanced efficiency in spectrum utilization [4, 5].

There are many methods used for frequency reconfiguration, and among them, the technique of integrating PIN diodes stands out as one of the common solutions; these diodes are integrated into the antenna's radiation elements, feed network, or ground plane, and their characteristics are controlled by adjusting their switching states [6, 7]. Researchers proposed an antenna integrating three semi-circular defected ground structures (DGS) [8], triple-intersecting DGS [9], and a circular DGS [10], each integrated with different numbers of switches to enable multiple frequency bands. In [11], PIN diodes integrated into triangular monopoles with a partial ground plane containing etched parasitic strips enabled switching between narrowband and ultra-wideband (UWB).

As wireless devices continue to evolve and demand for high-data-rate communication increases, congestion within microwave and millimeter-wave (mmWave) frequency bands has accelerated research into THz communications. THz waves have emerged as a promising solution for terabit-per-second communication systems [12].

Many antenna types, such as dipole, bow-tie, Yagi, dielectric resonator, fractal, and patch antennas, have been proposed and studied for THz systems [13, 14]. For contemporary communication systems that demand both flexibility and excellent performance, the capacity to dynamically alter antenna properties, such as operating frequency and radiation pattern, is crucial [13]. However, traditional reconfiguration mechanisms based on PIN diodes face fundamental obstacles at THz frequencies, specifically in the transition band between THz and infrared; these limitations are metal diffusion, impedance mismatch between the antenna and diode, and deterioration of the rectifier diode's operational performance [15]. Accordingly, THz applications require developing alternative switching technologies; graphene stands out as a promising and ideal choice among available materials, thanks to its complex conductivity, which can be precisely tuned, enabling an effective and efficient switching mechanism in THz devices [16].

Graphene, a single-layer carbon material with a hexagonal crystal lattice, has exceptional electrical properties that help

* Corresponding authors: Khalid Subhi Ahmad (jarkovo_1988@ntu.edu.iq); Muhammad Inam Abbasi (inamabbasi@utem.edu.my).

TABLE 1. Geometrical parameters of the suggested antenna (μm).

Parameter	Wg	Lg	W	L	Wf	Lf	$l1$	$l2$	$l3$	$l4$
Value	268	240	154	120	24	69	110	102.5	81	81
Parameter	$l5$	$l6$	$l7$	a	b	c	d	e	f	s
Value	55	85	55	31	24	60	10	20	40	5

overcome multiple technical obstacles facing THz technology. Graphene facilitates the propagation of surface plasmon-polariton waves in the THz band because of its strong field-effect behavior and high electron mobility. In THz reconfigurable antenna systems, these features are very advantageous for electrical tuning [17]. Graphene has multiple uses in THz antennas; it can be employed as a ground layer, a radiating element, or a switching layer. Its variable surface conductivity, controlled by the applied chemical potential (μ_c), offers broad reconfiguration opportunities, as adjusting the bias voltage applied to the graphene enables dynamic control of the antenna's operating frequency, radiation pattern, and polarization [18]. In the literature, studies on THz antenna designs, including single-band [18], dual-band [19], and multi-band [12], confirm graphene's essential role in reconfigurability in THz communication devices. By regulating graphene conductivity in electrical means, several graphene-assisted THz antennas, including Yagi-Uda, ring, planar-slot, and bow-tie structures, demonstrated frequency tunability and pattern reconfiguration [19–23]. In addition, [24] demonstrated a reconfigurable Vivaldi antenna based on graphene that operates over 0.5–2 THz, enabling dynamic impedance and bandwidth control via graphene-silicon structures.

This work illustrates a graphene-based frequency-reconfigurable terahertz antenna (FRTA) operating over a wide frequency range of 0.2–2.5 THz. Frequency reconfiguration is achieved by electrically tuning the chemical potential of integrated graphene switches, enabling effective control of the antenna resonant frequencies.

2. APPROACH TO THE DESIGN OF THE PROPOSED ANTENNA

The suggested antenna is displayed in Fig. 1, occupying an area of 240 μm in length (L), 268 μm in width (W), and 10 μm in thickness (h), based on the Rogers RO3003 substrate thickness. The employed substrate has a relative dielectric constant

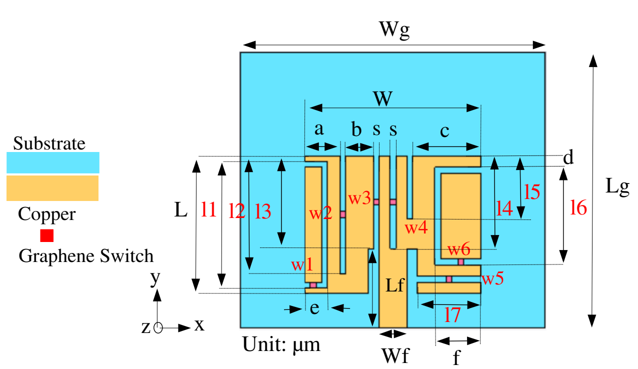

FIGURE 1. The configuration of the proposed THz patch antenna.

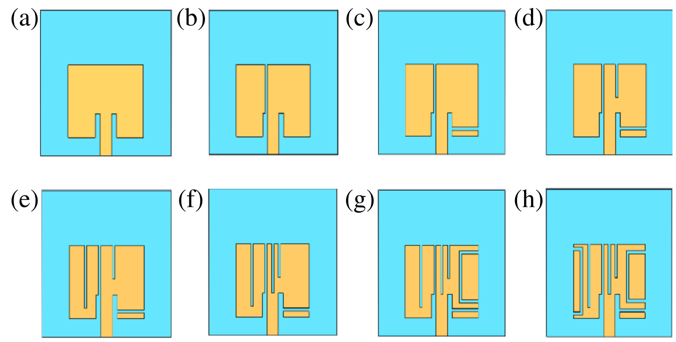

FIGURE 2. Development stages of the proposed FRTA from S1 to S8: (a) conventional patch antenna (S1), (b) S2, (c) S3, (d) S4, (e) S5, (f) S6, (g) S7, and (h) S8.

of 3 and a loss tangent of 0.001. The feed line has a length of $Lf = 69$ μm and a width of $Wf = 24$ μm. The proposed antenna is a patch antenna with longitudinal and vertical slots. Table 1 presents the complete set of antenna parameters. Based on the structural framework shown in Fig. 1, Figs. 2(a)–(h) illustrate the developmental stages of the proposed antenna design. The development of this framework was primarily based on an optimized aperture-distribution methodology for the radiating patch. These carefully planned apertures enhance the antenna's frequency response, enabling multiple resonant frequencies while maintaining the framework's compact dimensions.

In Figs. 2(a)–(h), the evolution of the proposed antenna is through eight stages (S1–S8). In the primary stage (S1), a conventional rectangular microstrip patch antenna with the previously mentioned dimensions is designed on a Rogers RO3003 substrate. The antenna resonates at 0.689 THz with an impedance bandwidth of 0.025 THz over 0.677–0.702 THz, equivalent to a fractional bandwidth of 3.63%. The obtained reflection coefficient is −25.28 dB, while the realized gain and radiation efficiency are 3.27 dB and 44%, respectively. To change the effective surface current distribution and produce more resonant modes, vertical and horizontal slots are gradually added to the radiating patch in stages S2–S8. Improvements in radiation efficiency, bandwidth, gain, and impedance matching are attained as the antenna structure changes. Additionally, multiband operation is enabled while preserving small antenna dimensions by progressive slot inclusion.

Figures 3(a)–(c) compare stages S1–S8 in terms of reflection coefficient, gain, and radiation efficiency. The peak gain values of the antenna throughout the evolution stages are as follows: 3.27 dB at 0.6896 THz for stage S1, 6.87 dB at 3.3977 THz for stage S2, 9.21 dB at 2.6123 THz for stage S3, 7.57 dB at 2.3054 THz for stage S4, 7.30 dB at 3.1403 THz for stage S5,

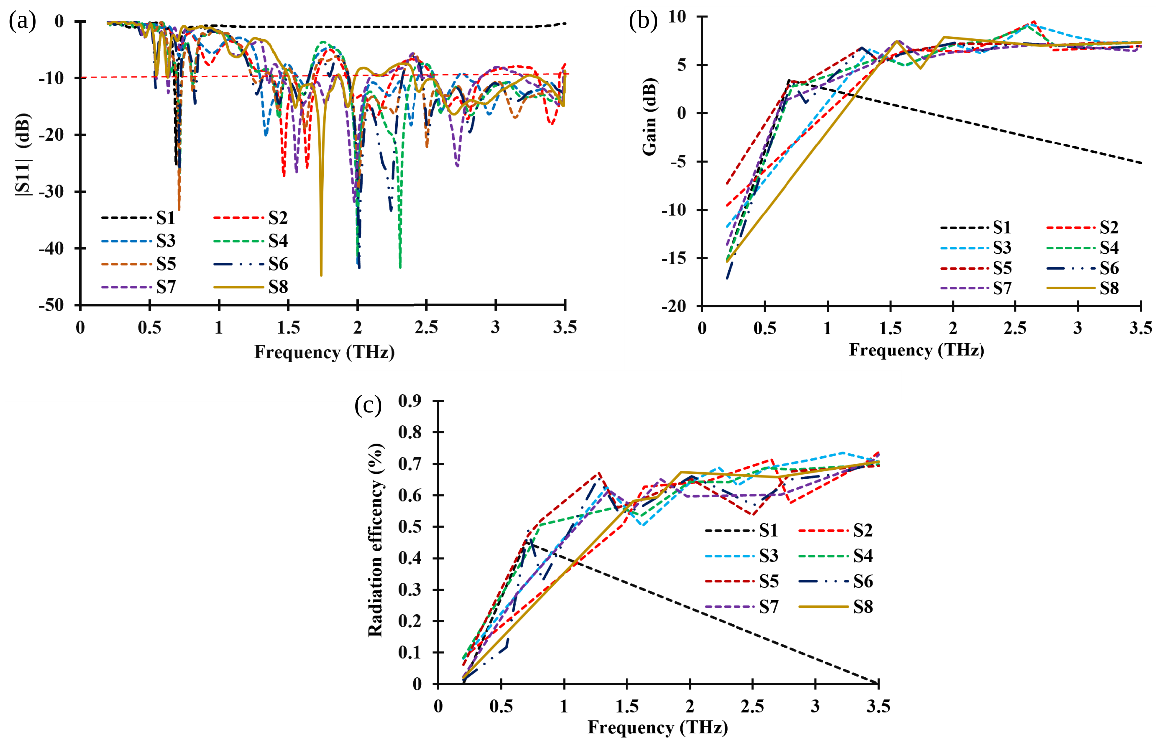

FIGURE 3. Simulated results of antenna stages 1–8: (a) S_{11}, (b) radiation efficiency (linear scale), and (c) gain (dB).

7.30 dB at 2.0117 THz for stage S6, 7.60 dB at 1.5563 THz for stage S7, and 7.87 dB at 1.929 THz for stage S8, as shown in Fig. 3(b). The radiation efficiencies obtained for the proposed antenna throughout the operating bands vary according to the design stage and resonant frequency, reaching maximum values of approximately 44%, 70.44%, 71.21%, 68.20%, 68.39%, 65.08%, 70.90%, and 70.58%, respectively, as illustrated in Fig. 3(c).

2.1. Graphene-Based Frequency Reconfiguration Mechanism and Modeling

The resonant frequency of the proposed FRTA is controlled using six graphene switches ($w1$–$w6$), embedded within slots e, $l2$, $l3$, $l4$, $l7$, and f, respectively, as illustrated in Fig. 1. Switches $w1$ and $w6$ are positioned 5 µm and 15 µm away from the left and right edges of the patch antenna within slots e and f, respectively. Meanwhile, switches $w2$–$w5$ are located at the centers of slots $l2$, $l3$, $l4$, and $l7$. The corresponding slot lengths are $e = 20$ µm, $l2 = 103$ µm, $l3 = 81$ µm, $l4 = 81$ µm, $l7 = 40$ µm, and $f = 55$ µm. Multiple frequency-reconfigurable modes are achieved by integrating graphene-based switching elements into the patch structure. Electrostatic biasing is used to implement the switching process, in which an external DC bias voltage controls the graphene chemical potential (μ_c). Changes in the chemical potential control the modification of graphene's surface conductivity according to the Kubo model, leading to changes in the actual current distribution and the antenna resonant characteristics. Graphene switches adjust the resonant frequencies and operating modes by electrically connecting or disconnecting specific regions of the metal patch, enabling 11 distinct operating states (ON/OFF).

Graphene occupies a leading position in fast electronics and electromagnetic systems research thanks to its exceptional electrical properties; its unique band structure and supercharged carrier mobility form a key foundation for increasing the efficiency of THz devices, interconnect lines, and field-effect transistors (FETs). The angular frequency ω, chemical potential μ_c, temperature T, and scattering rate Γ all affect graphene's surface conductivity, σ_g (ω, μ_c, Γ, T). The formula for the relaxation time τ is $\tau = 1/(2\Gamma)$ [25].

Graphene conductivity can be described using the Kubo formula, which comprises intraband (σ_{intra}) and interband (σ_{inter}) conductivity components. The intraband contribution is mainly associated with free-carrier transport, whereas the interband contribution corresponds to electron transitions between the valence and conduction bands. In the THz frequency range, graphene's conductivity is predominantly intraband, and the interband contribution becomes more significant at higher frequencies [26].

The proposed antenna primarily operates using discrete ON/OFF switching states corresponding to different graphene conductivity conditions. In addition, continuous conductivity tuning is investigated by varying the chemical potential (μ_c) to analyze resonance redistribution and impedance variations under intermediate bias conditions. The present work mainly focuses on the electromagnetic behavior of the graphene-enabled antenna structure; therefore, the detailed biasing network and its associated parasitic effects are beyond the scope of the current study. In practice, high-impedance or minimally invasive biasing structures may be employed to reduce disturbances to THz radiation characteristics.

$$\sigma_g = \sigma_{intra} + \sigma_{inter} \tag{1}$$

$$\sigma_{intra} = \frac{-je^2 k_B T}{\pi\hbar\,(\omega - 2j\Gamma)} \left(\frac{\mu_c}{k_B T} + 2\ln\!\left(e^{-\frac{\mu_c}{k_B T}} + 1\right)\right) \tag{2}$$

$$\sigma_{inter}(\omega\cdot\mu_c\cdot\Gamma\cdot T) = j\frac{e^2}{4\pi\hbar}\ln\left(\frac{2\,|\mu_c| - (\omega+2j\Gamma)\hbar}{2\,|\mu_c| + (\omega+2j\Gamma)\hbar}\right) \tag{3}$$

where e denotes the electron charge; $\hbar$ is the reduced Planck's constant ($\hbar = 1.055 \times 10^{-34}$ J·s); k_B is the Boltzmann constant ($k_B = 1.38 \times 10^{-23}$ J/K); and $j = \sqrt{-1}$. The chemical potential (μ_c) can be controlled by applying an electrostatic bias field, particularly at THz frequencies. As μ_c increases, the real and imaginary parts of graphene's complex surface impedance ($Zs = 1/\sigma$) decrease. Consequently, graphene's conductivity and surface impedance can be dynamically tuned by varying μ_c. Due to its dynamic surface response in the THz band and exceptionally high carrier mobility, graphene is considered a promising material for THz reconfigurable antenna applications and high-speed signal-processing systems [26].

3. RESULTS AND ANALYSIS OF THE PROPOSED FRTA

The proposed FRTA was analyzed using Computer Simulation Technology (CST) Studio Suite 2022. Impedance matching is governed by the material wave impedance, which depends on the combined effects of permittivity (ε) and permeability (μ). In this work, Rogers RO3003 was selected as the substrate material due to its nonmagnetic nature ($\mu_r = 1$). Therefore, the effect of permeability on impedance matching is negligible. Instead, impedance tuning is achieved through the electrically controllable surface conductivity of graphene integrated into the antenna structure. Graphene's electrical tunability enables frequency reconfiguration without modifying the substrate properties.

By leveraging graphene's plasmonic properties, the proposed antenna achieves exceptional electromagnetic field exclusivity and dynamically tunable electrical features. Dynamic modulation of graphene's chemical potential controls its surface conductivity, enabling frequency reconfiguration and improved impedance matching. Furthermore, due to its lower energy loss rate compared to conventional metallic structures at THz frequencies, graphene is an ideal choice for reconfigurable THz antenna applications [12].

Given that graphene's surface conductivity is related to its chemical potential, any change in μ_c directly leads to modifying resistive and reactive components of the graphene layer. When the chemical potential is high, the graphene sheet has low impedance and minimal loss, showing ON-state behavior. On the other hand, at low chemical potential, the graphene layer exhibits higher impedance and reduced surface current density, representing the OFF state. This switching operation closely resembles the operation of PIN diodes in conventional radio frequency (RF) reconfigurable antennas [18].

Since graphene's surface conductivity depends on its chemical potential (μ_c), tuning μ_c modifies its resistive and reactive characteristics. High μ_c results in a low-impedance, low-loss ON state, whereas low μ_c produces a high-impedance OFF state with reduced surface current density. This behavior is analogous to the switching operation of PIN diodes in conventional RF reconfigurable antennas [18]. Accordingly, two chemical potential levels, $\mu_{c1} = 0$ eV and $\mu_{c2} = 4$ eV, were employed to realize OFF and ON states, respectively. A $5 \times 5 \times 5\,\mu\mathrm{m}^3$ graphene sheet was used for simulations at a temperature of 300 K with a relaxation time (τ) of 0.1 ps. To enable frequency reconfigurability, six single-layer graphene switches were integrated into the slotted patch structure. Resonant frequencies can be changed by dynamically adjusting the antenna's effective electrical length and surface-current distribution by switching graphene elements between ON and OFF states.

The proposed antenna demonstrates simultaneous multiband and multimode operation across all 11 switching configurations (C1–C11), generated through different ON/OFF combinations of the six graphene switches. Over a broad frequency range from 0.288 to 2.501 THz, the antenna achieves dynamically reconfigurable resonances. Graphene-loaded slots with normalized dimensions ($e = 0.019\lambda_0$, $l_2 = 0.0987\lambda_0$, $l_3 = 0.078\lambda_0$, $l_4 = 0.078\lambda_0$, $l_7 = 0.0529\lambda_0$, and $f = 0.0385\lambda_0$) offer a broad frequency tuning range surpassing 158.6% with regard to the lowest operational frequency of 0.288 THz. These slots modify the effective electrical length and, as a result, vary the resonant modes through bias-controlled modulation of graphene conductivity.

The suggested antenna enables multiband operation and wide-range frequency reconfiguration from lower THz bands up to 2.5 THz, as demonstrated by S_{11} characteristics summarized in Tables 2 and 3, supporting adaptive and multi-standard THz communication systems.

Effective frequency reconfigurability is achieved by intentionally keeping slot ($l5$) uncovered by graphene. This passive slot provides a stable resonant element, whereas covering all slots with graphene would cause simultaneous resonance shifts during biasing, resulting in mixed or unstable multiband responses. The interaction between the fixed resonance generated by the passive slot and the tunable resonances produced by the graphene-covered slots enables distinct multiband operating states. From a plasmonic perspective, the uncovered slot does not support tunable graphene-induced resonances and therefore maintains a bias-independent resonance that acts as a stable reference interacting with tunable surface plasmon polariton modes.

According to Table 3, the proposed FRTA operates in multiple resonant states for configurations C1–C11, spanning a frequency range from 0.288 to 2.501 THz and featuring several multiband operating modes. The reflection coefficient ranges from −49.56 dB to −11.17 dB, indicating adequate to good impedance matching, whereas the simulated impedance bandwidth spans from 1.52% to 29.72%. Radiation efficiency varies with switching mode because each graphene state reshapes the antenna's effective electrical length, resonant mode, and current distribution, leading to different impedance-matching conditions. Furthermore, graphene's finite conductivity causes significant ohmic losses that reduce radiation efficiency in some modes.

TABLE 2. ON/OFF states of graphene switches (d1–d6) for configurations C1–C11.

Case No.	$w1$	$w2$	$w3$	$w4$	$w5$	$w6$	Operating frequencies
C1	0	0	0	0	0	1	0.372, 0.682, 0.790, 0.867, 1.731, 2.028, 2.482
C2	0	0	0	0	1	0	0.684, 1.568, 1.745, 1.944, 2.165, 2.446
C3	0	0	1	1	0	0	0.341, 0.999, 1.474, 1.584, 1.772, 2.043
C4	0	1	1	1	0	0	0.401, 1.071, 1.472, 1.700, 2.048
C5	1	0	0	1	1	0	0.660, 0.723, 1.474, 1.592, 1.798, 1.997, 2.228
C6	1	0	1	0	0	1	1.712, 1.973, 2.093
C7	1	1	0	1	0	0	1.169, 1.364, 1.575, 1.625, 1.812, 1.964, 2.172
C8	1	1	0	1	0	1	0.368, 0.694, 1.359, 1.604, 1.817, 2.192, 2.499
C9	1	1	0	1	1	1	0.370, 0.694, 1.606, 1.827, 2.201, 2.501
C10	1	1	1	0	1	0	0.288, 0.540, 0.792, 1.364, 1.452, 1.678, 1.752, 2.108
C11	1	1	1	1	1	0	0.320, 0.790, 1.061, 1.457, 1.678, 2.067
Switch status	0 = OFF state ($\mu_{c1} = 0$ eV); 1 = ON state ($\mu_{c2} = 4$ eV)						

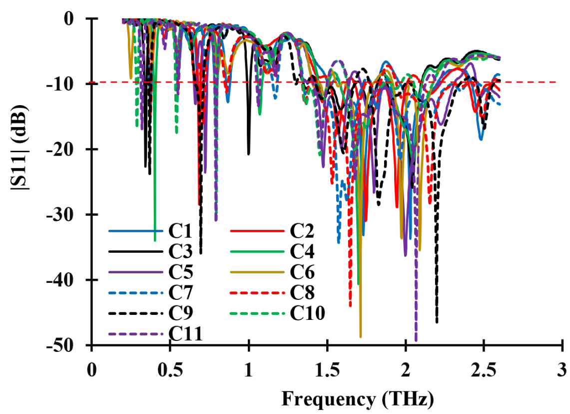

FIGURE 4. Simulated gains for configurations C1–C11.

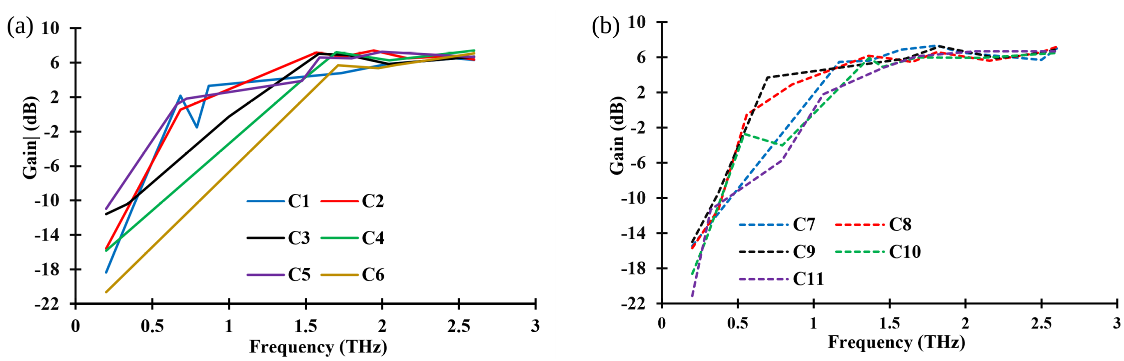

FIGURE 5. Simulated gains for configurations: (a) C1–C6 and (b) C7–C11.

The simulated S_{11} response is employed to assess the FRTA's frequency tunability. The resonance characteristics for all configurations are summarized in Table 3 and illustrated in Fig. 4, while the corresponding gain responses are presented in Fig. 5. Furthermore, the proposed antenna achieves a gain ranging from -14.81 dB to 7.41 dB across the tuning range. Among all configurations, C9 achieves the highest resonance frequency of 2.501 THz, whereas C10 exhibits the lowest resonance frequency of 0.288 THz. Finally, based on graphene patch impedance states, the antenna supports 11 distinct operating configurations. The radiation efficiency varies from 1.16% in C10 to 74% in C5.

To avoid redundancy and unnecessary increases in content size from reviewing radiation diagrams and surface current distributions for (63) resonant frequencies (distributed across (11) switching cases of the proposed antenna), only six representative switching models were selected.

Figures 6(a)–(f) show simulated radiation patterns of the proposed FRTA for configurations C1, C3, C4, C6, C10, and C11 in the E-plane (YZ) and H-plane (XZ). These configurations correspond to resonant frequencies of 0.372, 0.999,

TABLE 3. Summary of the simulated performance characteristics of configurations C1–C11.

No.	fr (THz)	S_{11} (dB)	BW Range	BW%	Gain (dB)	Eff. (%)
C1	0.372, 0.682, 0.790, 0.867, 1.731, 2.028, 2.482	−15.93, −15.21, −15.21, −12.8, −33.13, −33.67, −18.52	(0.368–0.380), (0.670–0.692), (0.780–0.800), (0.860–0.874), (1.580–1.822), (1.970–2.198), (2.424–2.500)	3.21, 3.23, 2.53, 1.62, 14.23, 10.94, 3.09	−10.28, 2.17, −1.49, 3.33, 4.80, 5.81, 6.51	2.40, 39.40, 16.00, 45.7, 0.24, 61.80, 56.00
C2	0.684, 1.568, 1.745, 1.944, 2.165, 2.446	−28.43, −17.60, −30.93, −28.83, −11.43, −14.27	(0.674–0.692), (1.516–1.620), (1.678–1.850), (1.870–2.006), (2.106–2.224), (2.406–2.500)	2.64, 6.63, 9.75, 7.01, 5.45, 3.83	0.56, 7.17, 6.67, 7.41, 6.48, 6.80	33.00, 54.90, 64.70, 67.00, 67.00, 55.40
C3	0.341, 0.999, 1.474, 1.584, 1.772, 2.043	−22.65, −20.75, −12.44, −13.89, −13.77, −25.88	(0.336–0.348), (0.990–1.010), (1.448–1.676), (1.716–1.817), (1.884–2.100)	3.5, 2.0, 14.71, 5.77, 10.83	−10.37, −0.27, 3.17, 7.02, 6.90, 5.84	2.70, 19.82, 47.00, 57.00, 66.46, 62.56
C4	0.401, 1.071, 1.472, 1.700, 2.048	−33.99, −14.68, −12.51, −40.59, −21.86	(0.396–0.406), (1.061–1.083), (1.445–1.505), (1.582–1.788), (1.906–2.105)	2.39, 2.24, 4.06, 12.34, 9.86	−12.50, −2.19, 3.94, 7.24, 6.30	7.60, 32.00, 47.46, 73.83, 60.00
C5	0.660, 0.723, 1.474, 1.592, 1.7984, 1.997, 2.228	−13.07, −23.56, −22.73, −19.8, −26.61, −36.30, −16.20	(0.654–0.666), (0.714–0.734), (1.412–1.638), (1.714–2.312)	1.82, 2.76, 14.82, 14.82, 29.72, 29.72	1.14, 1.84, 3.87, 6.61, 6.52, 7.27, 7.00	28.52, 41.41, 47.00, 52.50, 62.00, 74.00, 69.50
C6	1.712, 1.973, 2.093	−48.74, −33.65, −35.43	(1.619–1.784), (1.920–2.021), (2.046–2.173)	9.74, 5.13, 5.99	5.70, 5.35, 5.75	59.00, 60.94, 67.83
C7	1.169, 1.364, 1.575, 1.625, 1812, 1.964, 2.172	−12.2, −11.73, −34.35, −28, −13.73, −21.46, −14.94	(1.154–1.180), (1.350–1.382), (1.432–1.728), (1.780–1.850), (1.896–2.386)	2.23, 2.34, 18.73, 3.86, 22.90	5.45, 5.62, 6.88, 6.97, 7.33, 6.53, 6.20	39.65, 60.85, 54.7, 57, 66.00, 66.56, 64.00
C8	0.368, 0.694, 1.359, 1.604, 1.817, 2.192, 2.499	−22.49, −30.04, −10.90, −22.47, −34.56 −16.35	(0.363–0.375), (0.660–0.711), (1.347–1.376), (1.428–1.673), (1.757–2.343), (2.456–2.556)	3.36, 7.35, 2.11, 15.78, 28.56, 4.02	−9.79, 3.34, 5.70, 5.85, 5.95, 5.84, 6.45	3.18, 46.73, 51.85, 48.78, 66.43, 63.91, 56.94
C9	0.370, 0.694, 1.606, 1.827, 2.201, 2.501	−23.71, −35.89, −20.58, −28.48, −46.43, −16.80	(0.363–0.375), (0.654–0.712), (1.428–1.674), (1.770–1.998), (2.036–2.346), (2.456–2.561)	14.15, 8.50, 15.87, 12.10, 14.15, 4.21	−9.52, 3.69, 5.83, 7.22, 5.91, 6.51	3.37, 50.82, 48.00, 68.40, 65.50, 57.00
C10	0.288, 0.540, 0.792, 1.364, 1.452, 1.678, 1.752, 2.108	−16.73, −17.78, −30.72, −13.16, −20.85, −21.30, −16.76, −13.71	(0.284–0.291), (0.536–0.546), (0.784–0.800), (1.344–1.498), (1.632–1.860), (2.052–2.174)	2.50, 1.85, 2.02, 10.83, 10.83, 13.05, 5.77	−14.81, −2.69, −4.00, 5.95, 4.89, 6.00, 5.98, 5.92	1.16, 15.0, 9.64, 62.00, 53.00, 44.00, 48.00, 66.62
C11	0.32, 0.790, 1.061, 1.457, 1.678, 2.067	−16.84, −31.11, −13.44, −20, −24.72, −49.56	(0.315–0.324), (0.785–0.797), (1.052–1.071), (1.412–1.498), (1.635–2.127)	3.0, 1.52, 1.81, 5.94, 26.16, 26.16	−11.32, −5.74, 1.77, 4.8, 6.12, 6.69	2.3, 7.94, 33.0, 52.45, 45.67, 66.65
Switch status		0 = OFF State = $\mu_{c1} = 0$ eV, 1 = ON State = $\mu_{c2} = 4$ eV				

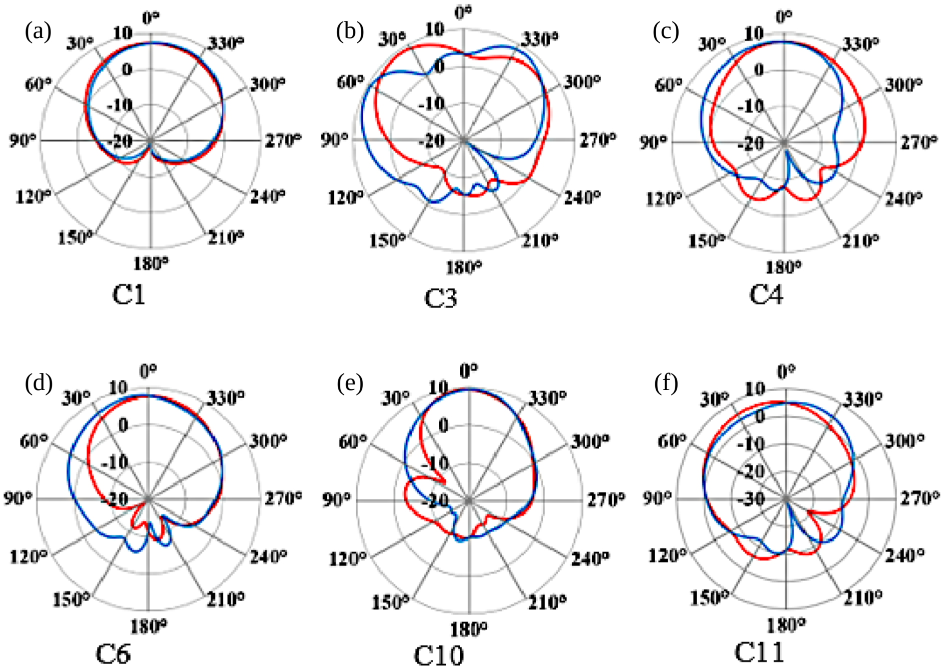

FIGURE 6. Simulated two-dimensional radiation patterns in the E ($\varphi = 0°$, in blue) and H ($\varphi = 90°$, in red) planes. The figure shows the selected configurations (C1, C3, C4, C6, C10, C11) at their corresponding resonant frequencies as follows: (a) configuration C1 at 0.372 THz, (b) configuration C3 at 0.999 THz, (c) configuration C4 at 1.472 THz, (d) configuration C6 at 1.712 THz, (e) configuration C10 at 2.108 THz, and (f) configuration C11 at 2.067 THz.

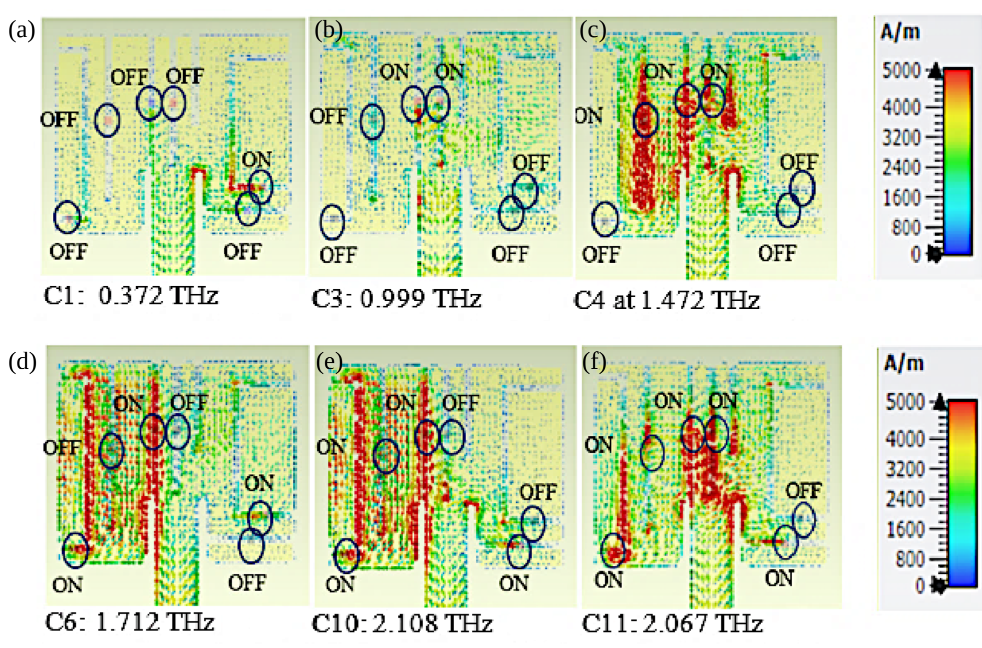

FIGURE 7. Surface-current distributions on top of the FRTA for the selected configurations C1, C3, C4, C6, C10 and C11, respectively: (a) C1 at 0.372 THz, (b) C3 at 0.999 THz, (c) C4 at 1.472 THz, (d) C6 at 1.712 THz, (e) C10 at 2.108 THz, and (f) C11 at 2.067 THz.

1.472, 1.712, 2.067, and 2.108 THz and show different switching states. The antenna mainly exhibits linear polarization. It keeps stable broadside radiation during frequency reconfiguration.

Figure 7 shows simulated surface-current distributions of the proposed FRTA for configurations C1, C3, C4, C6, C10, and C11 at chosen resonant frequencies of 0.372, 0.999, 1.472, 1.712, 2.067, and 2.108 THz. Graphene layers control the resonant current paths by reshaping the conductivity distribution on the radiating patch. Surface-current paths change based on graphene's conductivity changes, generating resonant frequencies specific to each switching state.

The influence of graphene chemical potential on the frequency-reconfigurable behavior of the proposed antenna

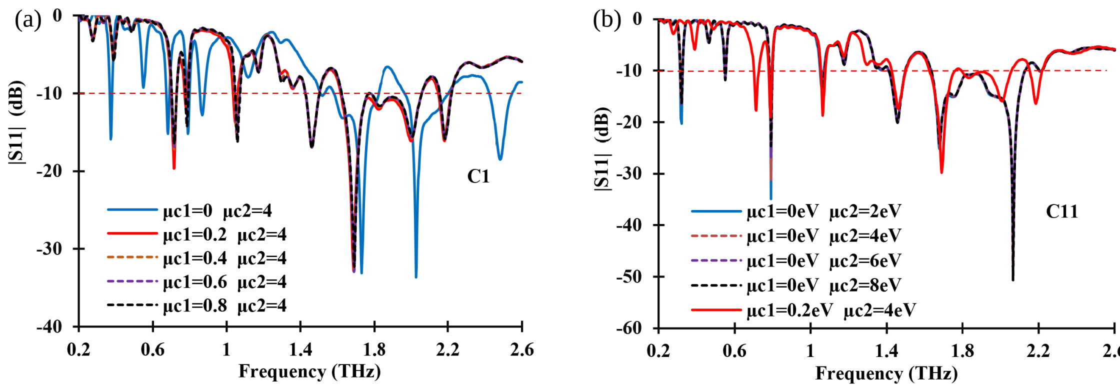

FIGURE 8. Effect of graphene bias potential on $|S_{11}|$: (a) variation of μ_{c1} from 0 to 0.8 eV with $\mu_{c2} = 4$ eV for configuration C1 and (b) variation of μ_{c2} from 2 to 8 eV for configuration C11, with μ_{c1} fixed at 0 eV except for the case $\mu_{c1} = 0.2$ eV and $\mu_{c2} = 4$ eV.

TABLE 4. FRTA response of configuration C1 under different graphene chemical potentials (0–0.8) eV.

State/Chemical Potential μ_c (eV)	Frequency	S_{11} (dB)	BW	BW (%)	Gain (dB)
C1, $\mu_{c1} = 0$, $\mu_{c2} = 4$	0.372, 0.682, 0.790, 0.867, 1.731, 2.028, 2.482	−15.93, −15.21, −15.21, −12.8, −33.13, −33.67, −18.52	(0.368–0.380), (0.670–0.692), (0.780–0.800), (0.860–0.874), (1.580–1.822), (1.970–2.198), (2.424–2.500)	3.21, 3.23, 2.53, 1.62, 14.23, 10.94, 3.09	−10.28, 2.17, −1.49, 3.33, 4.80, 5.81, 6.51
C1, $\mu_{c1} = 0.2$, $\mu_{c2} = 4$	0.713, 0.778, 1.047, 1.460, 1.685, 2.000, 2.1824	−19.68, −11.69, −13.77, −16.92, −32.82, −16.15, −16.10	(0.701–0.728), (0.773–0.785), (1.035–1.059), (1.426–1.500), (1.618–2.057), (2.148–2.216)	3.69, 1.54, 2.29, 5.08, 23.89, 23.89, 3.08	−0.96, −5.53, −2.75, 5.13, 6.62, 4.91, 4.92
C1, $\mu_{c1} = 0.4$, $\mu_{c2} = 4$	0.716, 0.783, 1.054, 1.462, 1.688, 2.004, 2.184	−17.34, −12.64, −15.17, −16.83, −32.82, −15.80, −15.93	(0.704–0.728), (0.776–0.788), (1.042–1.066), (1.426–1.500), (1.620–2.057), (2.153–2.218)	3.35, 1.53, 2.28, 5.08, 23.76, 23.76, 2.97	−0.44, −4.99, −2.30, 5.18, 6.73, 5.20, 5.05
C1, $\mu_{c1} = 0.6$, $\mu_{c2} = 4$	0.716, 0.783, 1.056, 1.462, 1.688, 2.004, 2.184	−16.88, −13.46, −15.71, −16.93, −32.94, −15.66, −15.82	(0.704–0.728), (0.776–0.790), (1.044–1.068), (1.428–1.500), (1.623–1.767), (1.781–2.057), (2.156–2.218)	3.35, 1.84, 2.27, 4.92, 8.50, 14.38, 2.85	−0.19, −4.51, −2.16, 5.22, 6.75, 5.20, 5.15
C1, $\mu_{c1} = 0.8$, $\mu_{c2} = 4$	0.716, 0.785, 1.059, 1.462, 1.690, 2.007, 2.184	−16.53, −14.36, −16.36, −17.07, −32.32, −15.56, −15.88	(0.704–0.728), (0.778–0.792), (1.047–1.071), (1.428–1.500), (1.623–1.767), (1.781–2.057), (2.156–2.218)	3.35, 1.83, 2.27, 4.92, 8.50, 14.38, 2.85	−0.10, −4.48, −0.53, 5.23, 6.79, 5.35, 5.20

TABLE 5. FRTA response in configuration C11 under different graphene chemical potentials (2–8) eV.

State/Chemical Potential μ_c (eV)	Frequency	S_{11} (dB)	BW	BW (%)	Gain (dB)
C11, $\mu_{c1} = 0$, $\mu_{c2} = 2$	0.320, 0.550, 0.790, 1.059, 1.457, 1.678, 2.067	−20.27, −10.84, −34.94, −13.26, −20.08, −25.21, −43.79	(0.315–0.324), (0.548–0.550), (0.783–0.795), (1.049–1.068), (1.412–1.498), (1.632–2.129)	3.00, 0.44, 1.52, 1.81, 5.94, 26.64, 26.64	−11.47, −2.40, −5,95, 1.65, 4.74, 6.07, 6.65
C11, $\mu_{c1} = 0$, $\mu_{c2} = 4$	0.320, 0.790, 1.061, 1.457, 1.678, 2.067	−16.84, −31.11, −13.44, −20.00, −24.72, −49.56	(0.315–0.324), (0.785–0.797), (1.052–1.071), (1.412–1.498), (1.635–2.127)	3, 1.52, 1.81, 5.94, 26.16, 26.16	−11.32, −5.74, 1.77, 4.8, 6.12, 6.69
C11, $\mu_{c1} = 0$, $\mu_{c2} = 6$	0.320, 0.550, 0.790, 1.061, 1.457, 1.678, 2.067	−16.51, −11.83, −26.74, −13.58, −20.00, −24.29, −47.13	(0.315–0.324), (0.548–0.552), (0.785–0.797), (1.054–1.071), (1.412–1.498), (1.635–2.129)	3.00, 0.87, 1.52, 1.58, 5.94, 26.26, 26.26	−11.35, −2.19, −5,53, 1.8, 4.83, 6.01, 6.66
C11, $\mu_{c1} = 0$, $\mu_{c2} = 8$	0.320, 0.550, 0.790, 1.061, 1.457, 1.678, 2.067	−16.69, −11.64, −24.37, −13.67, −19.97, −23.99, −53.46	(0.315–0.324), (0.548–0.552), (0.785–0.797), (1.054–1.071), (1.412–1.498), (1.635–2.129)	3.00, 0.87, 1.52, 1.58, 5.94, 26.26, 26.26	−11.27, −2.21, −5,51, 1.79, 4.50, 5.97, 6.65
C11, $\mu_{c1} = 0.2$, $\mu_{c2} = 4$	0.713, 0.788, 1.064, 1.462, 1.690, 2.007, 2.187	−17.77, −19.03, −18.73, −17.39, −29.83, −15.94, −16.40	(0.701–0.725), (0.780–0.795), (1.054–1.076), (1.428–1.500), (1.628–1.760), (1.793–2.057), (2.156–2.218)	−0.88, −4.19, −1.62, 5.23, 6.74, 5.39, 5.24	26, 11, 16, 53, 60.67, 56.71, 65.27

was further investigated by varying the graphene bias beyond conventional ON/OFF states. The results indicate that small variations in the low-bias chemical potential (μ_{c1}) produce noticeable resonance shifts and changes in the number of operating bands, demonstrating high sensitivity to variations in graphene conductivity. In contrast, further increases in μ_{c1} beyond 0.2 eV result in only minor resonance variations, indicating near-saturation behavior of graphene switching elements, as shown in Fig. 8(a) and Table 4 for configuration C1. Similarly, variations in the high-bias chemical potential (μ_{c2}) mainly affect the impedance bandwidth and resonance behavior, whereas the resonant frequencies remain nearly unchanged at elevated bias levels, as illustrated in Fig. 8(b) and Table 5 for configuration C11.

To avoid excessive repetition, we present the detailed graphene chemical-potential analysis for representative configurations C1 and C11, while Table 6 summarizes responses of configurations C2–C10. It was found that identical tuning properties exist in configurations extending from C2 to C10 under various bias conditions of the graphene material. Modifying μ_{c1} from 0 to 0.2 eV across several configurations resulted in redistributing resonant frequencies, including frequency shifting up and down, the emergence of new resonant peaks, and variations in the total number of operating bands. It can be inferred from graphical patterns shown in Figs. 9(a)–(i) for configurations C2–C10 that the antenna's frequency response is closely related to graphene conductivity in the low-bias region, before the control shifts to saturation effects at high chemical potential levels.

The resonant displacement behavior is closely related to graphene position and its interaction with surrounding electromagnetic fields. In some configurations, increasing μ_{c1} produces downward resonance shifts due to enhanced capacitive-coupling effects. In other cases, upward or nonuniform reso-

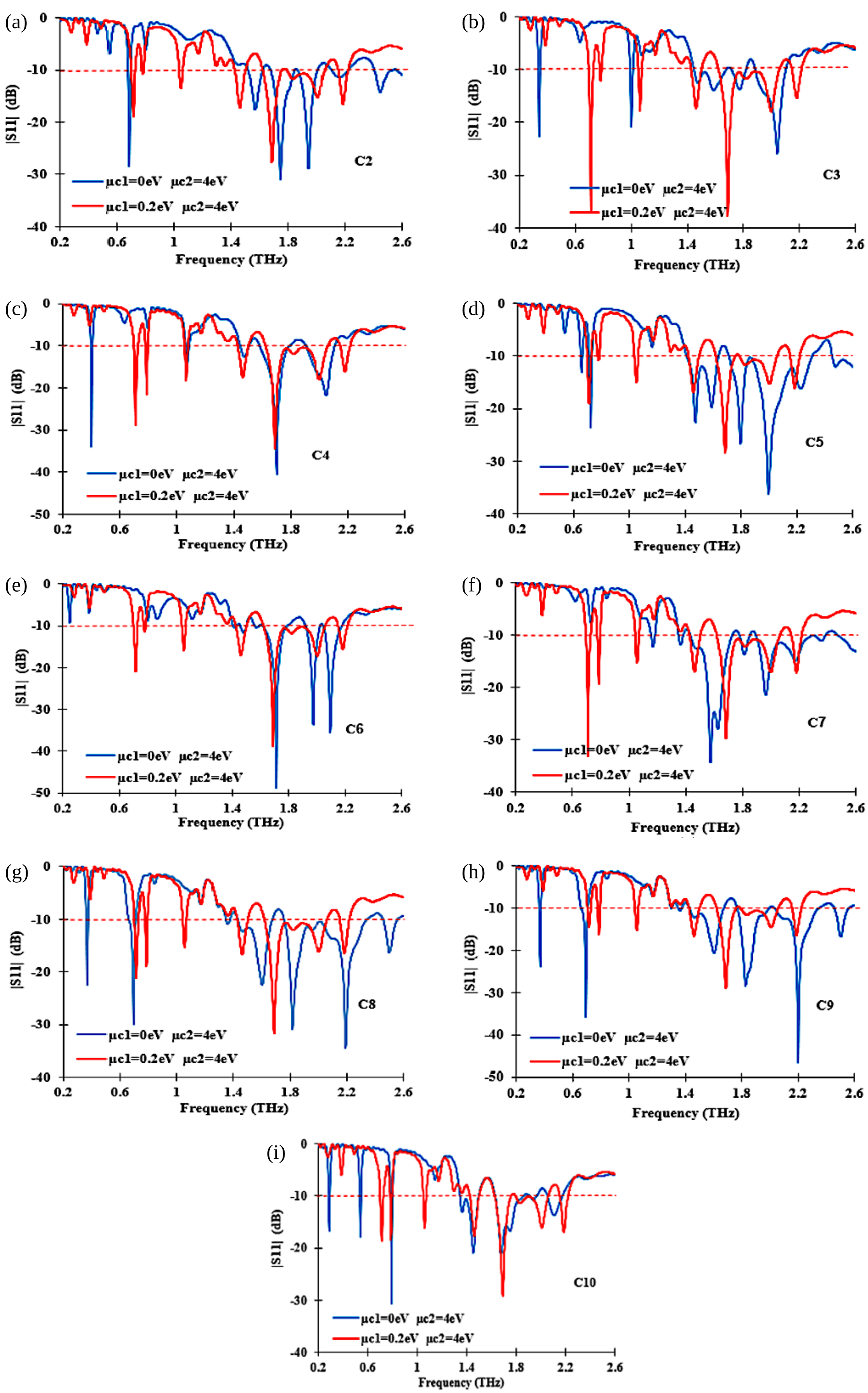

FIGURE 9. Simulated $|S_{11}|$ responses of configurations C2–C10 for $\mu_{c1} = 0$ and 0.2 eV with μ_{c2} fixed at 4 eV, illustrating resonance redistribution and variations in the operating bands under different graphene-bias conditions.

TABLE 6. Effect of graphene chemical-potential variation on the reconfigurable performance of configurations (C2–C10).

Config.	Bias Condition	No. of Bands	Max BW (%)	Max Gain (dB)
C2	$\mu_{c1} = 0$, $\mu_{c2} = 4$	6	9.75	7.41
C2	$\mu_{c1} = 0.2$, $\mu_{c2} = 4$	7	13.84	6.54
C3	$\mu_{c1} = 0$, $\mu_{c2} = 4$	5	14.71	7.02
C3	$\mu_{c1} = 0.2$, $\mu_{c2} = 4$	6	23.49	6.61
C4	$\mu_{c1} = 0$, $\mu_{c2} = 4$	5	12.34	7.24
C4	$\mu_{c1} = 0.2$, $\mu_{c2} = 4$	6	23.60	6.69
C5	$\mu_{c1} = 0$, $\mu_{c2} = 4$	4	29.72	7.27
C5	$\mu_{c1} = 0.2$, $\mu_{c2} = 4$	7	13.84	6.59
C6	$\mu_{c1} = 0$, $\mu_{c2} = 4$	3	9.74	5.75
C6	$\mu_{c1} = 0.2$, $\mu_{c2} = 4$	7	23.60	6.70
C7	$\mu_{c1} = 0$, $\mu_{c2} = 4$	5	22.90	7.33
C7	$\mu_{c1} = 0.2$, $\mu_{c2} = 4$	6	24.13	6.60
C8	$\mu_{c1} = 0$, $\mu_{c2} = 4$	6	28.56	6.45
C8	$\mu_{c1} = 0.2$, $\mu_{c2} = 4$	6	24.01	6.73
C9	$\mu_{c1} = 0$, $\mu_{c2} = 4$	6	15.87	7.22
C9	$\mu_{c1} = 0.2$, $\mu_{c2} = 4$	6	13.84	6.79
C10	$\mu_{c1} = 0$, $\mu_{c2} = 4$	6	13.05	5.98
C10	$\mu_{c1} = 0.2$, $\mu_{c2} = 4$	7	13.58	6.72

nance shifts are observed, which may be attributed to reduced capacitive coupling, altered current paths, and the increasing influence of inductive plasmonic effects.

In practice, a DC-biased network controls graphene switches by modulating their chemical potential to switch between ON/OFF states. Furthermore, these lines must be as short and narrow as possible, and located away from radiation edges to avoid parasitic coupling and unwanted secondary radiation.

Although simulation results of the proposed antenna are acceptable, its real-world implementation faces several manufacturing challenges, most notably growing graphene sheets using chemical vapor deposition, then transporting and shaping them by lithography before integrating them with metal conductors for electrical power. However, the difference in thermal expansion between graphene and the copper substrate during transport leads to defects such as wrinkles and cracks, which reduce charge-carrier flow and decrease antenna efficiency. Moreover, nanofabrication techniques used for terahertz antennas are characterized by their high cost, complexity, and the long time required to meet the required accuracy standards [27].

Table 7 compares the proposed reconfigurable THz antenna with several previously published reconfigurable THz antennas. The proposed antenna offers an ideal balance between structural complexity and frequency reconfigurability. Compared to a graphene-based terahertz antenna, the proposed antenna uses a moderate number of graphene switches, comparable to other highly reconfigurable designs. Although increasing the number of graphene switches doubles the complexity of the continuous bias (DC) network compared to systems with limited switching elements, it provides a wider tuning range and unique frequency options that surpass those in the referenced studies. Since all compared antennas rely on electrically controlled graphene conductivity, they are expected to show similar low-power electronic tuning characteristics. At the same time, practical switching speed is primarily determined by the bias circuitry rather than the antenna structure.

The proposed antenna demonstrates excellent reconfiguration flexibility and frequency agility. Most existing designs have a frequency-tuning capability below 120% and support fewer than 30 discrete operating frequencies or bandwidth regions. For example, the hybrid ring and Yagi-Uda antennas achieve tuning capabilities of only 27.9% and 58.5%, respectively, because of their limited tuning ranges and reduced reconfiguration flexibility. Although some reported THz antennas achieve higher peak gains, such as the graphene-loaded planar Vivaldi THz antenna in [24] with a gain of 11.5 dB, these improvements are generally achieved at the expense of larger size and increased structural complexity. In contrast, the proposed antenna maintains a compact size of $268 \times 240 \times 20$ µm while providing extensive frequency reconfigurability. In addition, the proposed antenna employs six graphene switching elements to achieve 63 unique operating frequencies and 58 bandwidth regions. This results in a frequency-tuning capability of 158.6%, which is the highest among the compared gaphene-based THz antennas, and enables an ultra-wide tuning range from 0.288 to 2.501 THz. The antenna also shows stable radiation characteristics with a maximum gain of 7.41 dB. Furthermore, the proposed antenna showed that radiation efficiency varied across reconfiguration conditions and reached moderate-

TABLE 7. Performance comparison of the proposed graphene-based THz frequency-reconfigurable antenna with previously reported works.

Ref.	Antenna type	Dimensions ($L \times W \times h$) (μm)	Operating Frequencies/BW Regions	Substrate	Tuning Range (THz)	Freq. Tuning Capability (%)	Max. Gain (dB)	Reconfiguration Method
[12]	Graphene-reconfigurable slot antenna	$268 \times 240 \times 20$	29/30	Rogers RO3003	0.52–2.06	119.7	7.8	Electrical biasing
[19]	Graphene-based microstrip patch antenna	$50 \times 50 \times 0.834$	5/5	Quartz	2.80–4.20	40	2	Electrical biasing
[20]	Planar Yagi-Uda antenna	$500 \times 700 \times 10$	5/5	SiO_2	0.243–0.444	58.5	4.53	Electrical biasing
[21]	Graphene bow-tie dipole antenna with AMC metasurface	$80 \times 80 \times 10.8$	12/12	SiO_2	2.08–3.10	39.4	7	Electrical biasing
[23]	Graphene-based hybrid ring antenna	$50 \times 50 \times 7$	17/16	FR-4	3.82–5.06	27.9	6	Electrical biasing
[24]	Graphene-loaded planar Vivaldi THz antenna	$500 \times 440 \times 10.02$	N/A/4	Quartz	0.50–2.00	120	11.5	Electrical biasing
This work	Copper slot antenna with six graphene sheets	$268 \times 240 \times 20$	63/58	Rogers RO3003	0.288–2.501	158.6	7.41	Electrical biasing

Note: The reported operating frequencies correspond to the unique resonance frequencies obtained after excluding repeated or overlapping resonances across different configurations listed in Table 2.

N/A: Indicates that the corresponding parameter was not reported in the referenced work.

AMC: Artificial Magnetic Conductor.

to-high values for most resonant frequencies. These results demonstrate that wide frequency tunability can be achieved while keeping acceptable radiation performance. For this reason, the proposed antenna is highly suitable for THz communication applications that require adaptive multiband operation and multi-state frequency reconfigurability.

Although ultra-wideband THz antennas can provide continuous spectral coverage, multiband frequency-reconfigurable antennas offer several important advantages for adaptive THz communication systems. Reconfigurable multiband operation enables selective activation of frequency bands, improving interference mitigation, reducing unnecessary spectral occupation, and enhancing spectral efficiency. In addition, discrete, tunable operating bands enable dynamic channel selection and adaptive spectrum utilization based on communication requirements and propagation conditions. Wideband THz antennas may also experience increased noise reception, stronger mutual interference, and more complex front-end filtering requirements across extremely large bandwidths. Therefore, the proposed graphene-based multiband reconfigurable antenna provides a flexible and energy-efficient alternative for future tunable THz communication systems.

4. CONCLUSION

The proposed graphene-based THz antenna demonstrated that tuning the graphene chemical potential can successfully achieve multiband frequency reconfigurability across a wide THz range. By integrating multiple graphene switches into the antenna structure, we realized several operating conditions while maintaining satisfactory impedance matching and radiation performance. The results indicate that graphene is a promising reconfiguration material for THz antennas, particularly at frequencies where conventional switching approaches become impractical. In addition, the proposed antenna provides a compact and structurally simple design while offering wide frequency tunability and a large number of operating conditions. Therefore, the antenna is well suited for adaptive beyond-6G THz communication systems requiring flexible multiband operation and frequency reconfigurability.

ACKNOWLEDGEMENT

This research was funded by funded by Universiti Teknikal Malaysia Melaka (UTeM) and Dominant Opto's Technologies through Matching Grant No. INDUSTRI

(URMG)/DOMINANT/FTKEK/2023/I00084. The authors would also like to thank the technical staff of UTeM for the support.

REFERENCES

[1] Suryapaga, V. and V. V. Khairnar, "Review on multifunctional pattern and polarization reconfigurable antennas," *IEEE Access*, Vol. 12, 90 218–90 251, 2024.

[2] Ahmad, K. S., F. C. Seman, S. A. Hamzah, K. Alhassoon, T. Saeidi, Z. Zakaria, and A. J. A. Al-Gburi, "Equivalent circuit model of antenna array utilizing an archimedean spiral sequential feed network for C-band applications," *Progress In Electromagnetics Research B*, Vol. 106, 151–165, 2024.

[3] Subhi, K., F. C. Seman, S. A. Hamzah, G. C. Hock, and S. M. Shah, "Circuit model for microstrip array antenna with defected ground structures for mutual coupling reduction and beamforming applications," *International Journal of Integrated Engineering*, Vol. 13, No. 1, 101–119, 2021.

[4] Ahmad, K. S., M. Z. A. A. Aziz, and A. J. A. Al-Gburi, "Compact frequency-reconfigurable slot patch antenna with gain enhancement via metasurface integration," *Optik*, Vol. 333, 172389, 2025.

[5] Bayer Keskin, S. E., S. Koziel, and S. Szczepanski, "Frequency reconfigurable PIN diode-based reuleaux-triangle-shaped monopole antenna for UWB/Ku band applications," *Scientific Reports*, Vol. 15, No. 1, 6555, 2025.

[6] Zhang, Y., Z. Han, S. Tang, S. Shen, C.-Y. Chiu, and R. Murch, "A highly pattern-reconfigurable planar antenna with 360° single- and multi-beam steering," *IEEE Transactions on Antennas and Propagation*, Vol. 70, No. 8, 6490–6504, 2022.

[7] Ahmad, K. S. and M. Z. A. A. Aziz, "Pattern reconfigurable planar antenna array based on two circular defected ground structure," *Przegląd Elektrotechniczny*, Vol. 7, No. 1, 52–55, 2021.

[8] Ahmad, K. S., M. Z. A. A. Aziz, and N. B. Abdullah, "A dual-band frequency reconfigurable antenna array based on reconfigurable defected ground structure," in *2020 IEEE International RF and Microwave Conference (RFM)*, 1–4, Kuala Lumpur, Malaysia, 2020.

[9] Ahmad, K. S. and M. Z. A. A. Aziz, "Frequency reconfigurable array antenna with modified circular slot," in *2022 IEEE International RF and Microwave Conference (RFM)*, 1–4, Kuala Lumpur, Malaysia, 2022.

[10] Ahmad, K. S. and M. Z. A. A. Aziz, "Frequency reconfigurable microstrip antenna array based on reconfigurable defected ground structure," *Przegląd Elektrotechniczny*, Vol. 8, No. 21, 114–120, 2021.

[11] Zhao, X., S. Riaz, and S. Geng, "A reconfigurable MIMO/UWB MIMO antenna for cognitive radio applications," *IEEE Access*, Vol. 7, 46 739–46 747, 2019.

[12] Ahmad, K. S. and A. J. A. Al-Gburi, "Graphene-based frequency reconfigurable slot antenna for terahertz applications," *Optik*, Vol. 330, 172343, 2025.

[13] Alibakhshikenari, M., E. M. Ali, M. Soruri, M. Dalarsson, M. Naser-Moghadasi, B. S. Virdee, C. Stefanovic, A. Pietrenko-Dabrowska, S. Koziel, S. Szczepanski, and E. Limiti, "A comprehensive survey on antennas on-chip based on metamaterial, metasurface, and substrate integrated waveguide principles for millimeter-waves and terahertz integrated circuits and systems," *IEEE Access*, Vol. 10, 3668–3692, 2022.

[14] Shi, Y., X. Zhang, Q. Qiu, Y. Gao, and Z. Huang, "Design of terahertz detection antenna with fractal butterfly structure," *IEEE Access*, Vol. 9, 113 823–113 831, 2021.

[15] Dragoman, M. and M. Aldrigo, "Graphene rectenna for efficient energy harvesting at terahertz frequencies," *Applied Physics Letters*, Vol. 109, No. 11, 113105, 2016.

[16] Wu, Y., M. Qu, L. Jiao, Y. Liu, and Z. Ghassemlooy, "Graphene-based Yagi-Uda antenna with reconfigurable radiation patterns," *AIP Advances*, Vol. 6, No. 6, 065308, 2016.

[17] Luo, Y., Q. Zeng, X. Yan, Y. Wu, Q. Lu, C. Zheng, N. Hu, W. Xie, and X. Zhang, "Graphene-based multi-beam reconfigurable THz antennas," *IEEE Access*, Vol. 7, 30 802–30 808, 2019.

[18] Kiani, N., F. T. Hamedani, and P. Rezaei, "Implementation of a reconfigurable miniaturized graphene-based SIW antenna for THz applications," *Micro and Nanostructures*, Vol. 169, 207365, 2022.

[19] Moradi, K., A. Pourziad, and S. Nikmehr, "A frequency reconfigurable microstrip antenna based on graphene in Terahertz Regime," *Optik*, Vol. 228, 166201, 2021.

[20] Liu, Q., R. Zhong, B. Xu, J. Dong, G. Teng, K. Zhong, Z. Wu, K. Zhang, M. Hu, and D. Liu, "Terahertz reconfigurable planar graphene hybrid Yagi-Uda antenna," *Nanomaterials*, Vol. 15, No. 7, 488, 2025.

[21] Varshney, A. K., N. P. Pathak, and D. Sircar, "Low-profile frequency reconfigurable graphene-based dipole antennas loaded with wideband metasurface for THz applications," *Plasmonics*, Vol. 17, No. 6, 2351–2363, 2022.

[22] Liang, F., Z.-Z. Yang, Y.-X. Xie, H. Li, D. Zhao, and B.-Z. Wang, "Beam-scanning microstrip quasi-Yagi-Uda antenna based on hybrid metal-graphene materials," *IEEE Photonics Technology Letters*, Vol. 30, No. 12, 1127–1130, 2018.

[23] Moradi, K., A. Pourziad, and S. Nikmehr, "An efficient graphene-based reconfigurable terahertz ring antenna design," *AEU — International Journal of Electronics and Communications*, Vol. 149, 154177, 2022.

[24] Poorgholam-Khanjari, S. and F. B. Zarrabi, "Reconfigurable Vivaldi THz antenna based on graphene load as hyperbolic metamaterial for skin cancer spectroscopy," *Optics Communications*, Vol. 480, 126482, 2021.

[25] Xu, Z., X. Dong, and J. Bornemann, "Design of a reconfigurable MIMO system for THz communications based on graphene antennas," *IEEE Transactions on Terahertz Science and Technology*, Vol. 4, No. 5, 609–617, 2014.

[26] Gusynin, V. P. and S. G. Sharapov, "Transport of dirac quasiparticles in graphene: Hall and optical conductivities," *Physical Review B — Condensed Matter and Materials Physics*, Vol. 73, No. 24, 245411, 2006.

[27] Ullah, Z., G. Witjaksono, I. Nawi, N. Tansu, M. I. Khattak, and M. Junaid, "A review on the development of tunable graphene nanoantennas for terahertz optoelectronic and plasmonic applications," *Sensors*, Vol. 20, No. 5, 1401, 2020.